

Faculty of Science,
University of Technology, Sydney

PhD Thesis

Optical Properties of Transition-Metal-Doped GaN and ZnO for Spintronics Applications

Enno Malguth

Diplom-Physiker

Technische Universität Berlin, Germany

February 2008

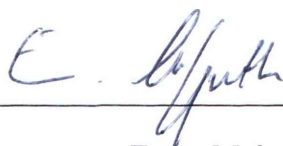
A thesis submitted in fulfilment of the requirements of the
degree of Doctor of Philosophy at the Faculty of Science,
University of Technology, Sydney



Certificate of Authorship and Originality

I certify that the work in this thesis has not previously been submitted for a degree nor has it been submitted as part of requirements for a degree except as fully acknowledged within the text.

I also certify that the thesis has been written by me. Any help that I have received in my research work and the preparation of the thesis itself has been acknowledged. In addition, I certify that all information sources and literature used are indicated in the thesis.

A handwritten signature in blue ink, appearing to read 'E. Malguth', is positioned above a horizontal line.

Enno Malguth

Acknowledgement

The work presented in this thesis was carried out under the supervision of Priv. Doz. Dr. Axel Hoffmann from TU-Berlin and Assoc. Prof. Matthew R. Phillips at the Microstructural Analysis Unit, Faculty of Science, University of Technology, Sydney. I wish to sincerely thank them for their competent guidance and support. Only through their invaluable expertise and countless stimulating discussions this pursuit became possible.

I would also like to thank Assist. Prof. Matthew H. Kane at University of Oklahoma, formerly at School of Electrical and Computer Engineering, Georgia Institute of Technology, Atlanta, for supplying the Mn doped GaN films. I am indebted to a number of talented people from TU-Berlin including but not limited to: Prof. Wolfgang Gehlhoff for carrying out the EPR measurements and for fruitful discussions, Dr. Lars Podlowski and Tobias Wolf for conducting the CAS experiments, Bernd Hausmann for preparing the Fe doped ZnO crystals, Till Warming for assistance with PLE experiments, Ronny Kirste and Ute Haboeck for Raman measurements, Stefan Werner, Rob McKenna and Christian Kristukat for assistance with PL measurements, Harald Scheel, Michael Meyer, Bernd Schöler and Markus Wagner. Additionally, I wish to thank Dr. Olaf Gehlhausen, Dr. Richard Wuhrer, Katie McBean, Dr. Scott Morgan, Steve Moody and Mark Berkahn from the Microstructural Analysis Unit. I would also like to thank the following individuals at the Georgia Institute of Technology and Georgia State University: Dr. Martin Strassburg, Shalini Gupta, William E. Fenwick, Prof. Nikolaus Dietz and Prof. Ian Ferguson. I thank Prof. Dominique Drouin and Nicolas Pauc at Université de Sherbrooke for using the LEO VP SEM and the low-temperature CL setup. Finally, I thank Dr. Xueping Xu for supplying high quality Fe doped GaN samples, and Dong-Du Mai and Jan Zenneck at Georg-August-Universität Göttingen for supplying Mn doped GaN films and performing PL measurements.

List of publications

Parts of this thesis have been published before in the following publications:

E. Malguth, A. Hoffmann and M. Phillips, “Fe in III-V and II-VI semiconductors,” *physica status solidi (b)* **245**(3): 455–480 (2008).

E. Malguth, A. Hoffmann, W. Gehlhoff, O. Gelhausen, M. R. Phillips and X. Xu, “Structural and electronic properties of Fe^{3+} and Fe^{2+} centers in GaN from optical and EPR experiments,” *Phys. Rev. B* **74**(16): 165202 (2006).

E. Malguth, A. Hoffmann and X. Xu, “Internal ${}^5\text{E} \rightarrow {}^5\text{T}_2$ transition of Fe^{2+} in GaN,” *Phys. Rev. B* **74**(16): 165201 (2006).

E. Malguth, A. Hoffmann, M. Phillips and W. Gehlhoff, “Fe-centers in GaN as candidates for spintronics applications,” in “Symposium Proceedings,” , (edited by M. Kuball, T. Myers, J. Redwing and T. Mukai), volume 892, 131–136, Mat. Res. Soc., Vol.892 (2006).

M. H. Kane, M. Strassburg, W. E. Fenwick, A. Asghar, J. Senawiratne, D. Azamat, E. M. Z. Hu, S. Graham, U. Perera, W. Gehlhoff, A. Hoffmann, N. Dietz, C. J. Summers and I. T. Ferguson, “Optical studies of MOCVD-grown GaN-based ferromagnetic semiconductor epilayers and devices,” *physica status solidi (c)* **3**(6): 2237–2240 (2006).

O. Gelhausen, E. Malguth, M. R. Phillips, E. M. Goldys, M. Strassburg, A. Hoffmann, T. Graf, M. Gjukic and M. Stutzmann, “Doping-level-dependent optical properties of GaN:Mn,” *Applied Physics Letters* **84**(22): 4514–4516 (2004).

O. Gelhausen, E. Malguth, M. R. Phillips, E. M. Goldys, M. Strassburg, A. Hoffmann, T. Graf, M. Gjukic and M. Stutzmann, “Optical properties

of Mn-doped GaN,” *Mat. Res. Soc. Symp. Proc.* **798**: 569–574 (2004).

E. Malguth, A. Hoffmann, W. Gehlhoff, M. H. Kane and I. T. Ferguson “Mn charge states in GaMnN as a function of Mn concentration and co-doping,” accepted for publication in *Mat. Res. Soc. Symp. Proc.* **1040** (2008).

E. Malguth, A. Hoffmann, S. Werner, M. H. Kane and I. T. Ferguson “Mn- and Fe- doped GaN for Spintronic Applications,” accepted for publication in *Mat. Res. Soc. Symp. Proc.* **1040** (2008).

Summary

Spin-based devices have the potential to take modern electronics and optoelectronics to the next level. So-called 'spintronics' exploit both the charge and the spin of an electron for data processing, transport and storage. A significant step towards the realisation of such devices would be to achieve room temperature ferromagnetic semiconductors. Theoretical works predict the possibility of room temperature ferromagnetism in the wide bandgap semiconductors GaN and ZnO doped with transition metals. The present models of spin-coupling in such dilute magnetic semiconductors require input in form of quantitative information on electronic states that arise from the introduction of transition metal ions into the host lattice. This work focuses on the detailed experimental investigation of such states in GaN and ZnO doped with different transition metals.

A large array of Fe, Mn and Ni doped GaN and ZnO samples with different doping levels and n-type and p-type co-doping were intensively studied by a wide range of experimental techniques. The investigation of Fe doped GaP, GaAs and InP provided valuable insights into the transient shallow acceptor state constituted by a hole bound to Fe^{2+} . The most significant results are summarised in the following:

A comprehensive literature review is presented on the Fe centre in III-V and II-VI semiconductors. Experimental and theoretical data that have been obtained over a few decades were reviewed thoroughly unveiling common phenomena that can be generalised to other TMs. The positions of established $\text{Fe}^{3+/2+}$ and $\text{Fe}^{2+/1+}$ levels were summarised allowing for predictions on the positions of further charge transfer levels based on the internal reference rule. The $\text{Fe}^{3+/4+}$ level has not been identified unambiguously in any of the studied materials. Detailed term schemes of the observed charge states in tetrahedral and trigonal crystal field symmetry are presented including fine structure, isotope effects and a dynamic Jahn-Teller effect.

By means of cathodoluminescence experiments Ni and Fe doping of HVPE-grown GaN was found to promote the formation of inhomogeneous regions with increased donor density and enhanced luminescence efficiency. In these regions richly structured cathodoluminescence patterns are observed at the surface.

By means of optical studies on high quality Fe doped GaN samples the electronic

structure of Fe^{3+} and Fe^{2+} was established in great detail. The effects of spin-orbit interaction, of the axial distortion of the crystal field in hexagonal GaN and of the Jahn-Teller coupling were successfully investigated. Both the Fe^{3+} centre and the Fe^{2+} centre were found to be stabilised against a dynamic Jahn Teller effect by the trigonal symmetry of the wurtzite lattice. A bound state with a binding energy of 50 ± 10 meV was identified as a hydrogenic state consisting of a hole localised at an Fe^{2+} centre. This $[\text{Fe}^{2+}, \text{h}]$ state represents a transient shallow acceptor state. It could be described by effective-mass-theory revealing an effective Bohr radius of 1.5 nm which may enable a long-range spin interaction via overlapping wavefunctions at relatively low Fe doping. The position of the $\text{Fe}^{3+/2+}$ acceptor level could be narrowed down to 2.863 ± 0.005 eV above the valence band maximum. Acting as a deep acceptor Fe incorporation was shown to quench the intrinsic yellow luminescence of GaN by lowering the Fermi level and passivating native donor states. Implications concerning the internal reference rule are discussed.

A deep understanding of the effective-mass-like state $[\text{Fe}^{2+}, \text{h}]$ could be obtained by temperature and stress dependent measurements on Fe doped GaP, GaAs and InP. Besides the ground state, the hole was observed in several excited hydrogenic states each involving different Fe^{2+} fine structure states. Particularly for the hydrogenic ground state, a weak exchange interaction was found between the hole Fe^{2+} core states. Due to finite p - d hybridisation of Fe orbitals with the valence band, a weaker binding energy was observed for the ground state than predicted by effective mass theory. Finally, with regard to the Fe^{3+} ground state, ${}^6\text{A}_1(\text{S})$, in GaP and InP, the hyperfine structure level Γ_8 was found to be above the Γ_7 level.

ZnO:Fe samples were prepared by Fe coating ZnO crystals, which were grown from the gas phase, and subsequent annealing under varying atmospheres. In these samples the internal $\text{Fe}^{2+}({}^5\text{E} \rightarrow {}^5\text{T}_2)$ transition was observed for the first time at 395.7 meV by means of Fourier transform infrared transmission spectroscopy. This value is in good agreement with the general trend in III-V and II-VI materials that the $({}^5\text{E} \rightarrow {}^5\text{T}_2)$ energy rises with an increasing degree of ionicity and decreasing lattice constant. No axial symmetry was found for the Fe^{2+} centre which is unusual for wurtzite ZnO. Possible reasons are discussed taking into account a strong Jahn-Teller effect, the non-constant c/a -ratio of ZnO and a high concentration of defects. Moreover, Fe-defect complexes and local vibrational modes could be identified.

A large array of GaN samples with varying Mn concentrations and n-type and p-type co-doping allowed for a systematic charge state tuning by shifting the Fermi level providing access to the oxidation states Mn^{2+} , Mn^{3+} and Mn^{4+} . The respective electronic structures were investigated by means of optical and magnetic techniques.

The Mn^{3+} centre and Mn^{4+} centre showed clear effects of degradation of crystal quality as a result of Mn, Si and Mg doping. A strong tendency was demonstrated for the formation of Mn-Mg complexes. A photoluminescence structure found around 1 eV in Mg co-doped GaN:Mn samples was proven to originate from Mn^{4+} involved in such complexes. A resonant Stokes process by secondary excitation and stimulated hole transfer was established in these Mn-Mg complexes. The $\text{Mn}^{3+/4+}$ donor and $\text{Mn}^{3+/2+}$ acceptor levels were found 1.15 eV and 1.65 eV above the VB maximum, respectively, compensating n-type and p-type doping. As a consequence, there is no reasonable chance to achieve high carrier concentrations in GaN:Mn, a precondition for free-carrier-mediated spin-coupling.

The results presented in this thesis contribute to the general understanding of transition-metal-related electronic states in III-V and II-VI semiconductors, particularly in GaN and ZnO. These new insights are valuable contributions to a targeted design of dilute magnetic semiconductors that will help to, one day, realise next-generation spintronic devices.

Contents

Acknowledgement	III
List of publications	IV
Summary	VI
List of Symbols and Abbreviations	XIII
List of Figures	XV
List of Tables	XX
1 Introduction	1
1.1 Spintronics	1
1.2 Motivation	2
1.3 Objectives	3
1.4 Approach	4
1.5 Thesis Structure	5
1.6 Spin-Coupling in Dilute Magnetic Semiconductors	6
2 Transition-Metal-Related Electronic States in Semiconductors	10
2.1 Deep Levels formed by Transition Metal Impurities	10
2.2 Charge Transfer Levels	11
2.2.1 Significance of Charge Transfer Levels	11
2.2.2 Determining the Position of the Charge Transfer Levels	14
2.3 Emergence of the Electronic Structure – Splitting of the <i>d</i> -Orbitals	14
2.3.1 The Free Ion	16
2.3.2 Crystalfield Splitting	18
2.3.3 Spin-Orbit Interaction	18
2.3.4 Trigonal Crystal Field in Axial Symmetry	19
2.3.5 Transition-Metal-Defect Complexes, Monoclinic Symmetry	19
2.3.6 Electron-Phonon Interaction – Jahn-Teller Effect	19

2.3.7	Isotope Effect	20
2.3.8	Selection Rules	21
2.4	Shallow Defect Levels – Hydrogenic States formed by Transition Metal Impurities	22
2.4.1	Observing and Describing the Shallow Hydrogenic state	23
3	Fe in III-V and II-VI Semiconductors – A Comprehensive Literature Review	24
3.1	Charge Transfer Levels	26
3.2	Implications of the found Charge Transfer Levels	27
3.2.1	The Fe^{3+} Centre	28
3.2.2	The Fe^{2+} Centre	39
3.2.3	The Fe^{1+} Centre	48
3.2.4	The $[\text{Fe}^{2+}, \text{h}]$ Bound State	49
3.3	Fe-Specific Vibrational Modes	52
3.4	Conclusion	52
4	Experimental Techniques	54
4.1	Samples	54
4.1.1	GaN:Fe	54
4.1.2	GaN:Ni	55
4.1.3	GaN:Mn	55
4.1.4	ZnO:Fe	55
4.1.5	Fe Doped GaAs, GaP, InP	56
4.2	Cathodoluminescence	56
4.3	Photoluminescence and Transmission Spectroscopy	56
4.4	Photoluminescence Excitation	57
4.5	Fourier Transform Infrared Spectroscopy	57
4.6	Calorimetric Absorption Spectroscopy	58
4.7	Zeeman Experiments	58
4.8	Electron Paramagnetic Resonance	58
4.9	Secondary Ion Mass Spectroscopy	59
4.10	Raman Spectroscopy	59
4.11	X-Ray Diffraction	60
4.12	SQUID Magnetometry	60
5	Preliminary Studies on Various Material Systems	62
5.1	Ni Doped GaN	62

5.1.1	Introduction	62
5.1.2	Structural and Optical Properties	62
5.1.3	Intra-Centre Transition of Ni	67
5.1.4	Conclusion	69
5.2	Fe Doped GaN	69
5.2.1	Structural and Electronic Uniformity	69
5.2.2	CL Pattern	73
5.2.3	The Fe^{3+} Luminescence	75
5.2.4	Conclusion	77
5.3	Mn Doped GaN	77
5.4	Fe Doped ZnO	81
5.5	Fe doped GaAs, GaP, InP	82
6	The Fe-Centre in GaN	83
6.1	Introduction	83
6.2	Structural Quality	83
6.2.1	EPR Experiments	83
6.2.2	Raman Investigations	84
6.3	Fe^{3+} in GaN	85
6.3.1	The ($^4\text{T}_1(\text{G})\text{—}^6\text{A}_1(\text{S})$) Transition	85
6.3.2	The Excited $^4\text{T}_1(\text{G})$ state	87
6.3.3	Vibrational Modes	89
6.3.4	Fe^{3+} -Related Complexes	91
6.3.5	Higher Excited States: $^4\text{T}_2(\text{G})$ and $^4\text{E}(\text{G})$	94
6.4	The $\text{Fe}^{3+/2+}$ Level	97
6.5	The Effective-Mass-Like State [Fe^{2+}, h]	97
6.6	The Term Scheme of Fe^{3+}	100
6.7	Excitation Processes	101
6.8	The Fe^{2+} Centre	105
6.9	Conclusion	112
7	Fine Structure of the [Fe^{2+}, h] Bound State	115
7.1	Experimental Results	116
7.1.1	Temperature Dependent Measurements	116
7.1.2	Uniaxial Stress Experiments	117
7.2	Discussion	120
7.2.1	The Ground State	120
7.2.2	The Bound state [$\text{Fe}^{2+}({}^5\text{E}), \text{h}$]	121

7.2.3	The Bound State $[\text{Fe}^{2+}(^5\text{T}_2), \text{h}]$	125
7.3	Conclusion	129
8	The Fe^{2+} Centre in ZnO	131
8.1	Introduction	131
8.2	Infrared Absorption of Fe Doped ZnO	131
8.3	The Fe^{2+} Centre in ZnO	134
8.4	Temperature Dependence of the $\text{Fe}^{2+}(^5\text{E} \rightarrow ^5\text{T}_2)$ Absorption	141
8.5	Discussion	142
8.6	Summary	144
9	The Mn-Centre in GaN	145
9.1	Introduction	145
9.2	Experimental Approach	146
9.3	Structural Properties	147
9.3.1	X-Ray Diffraction	147
9.3.2	Raman Spectroscopy	148
9.4	The Mn^{3+} Centre	149
9.5	The Mn^{2+} Centre	153
9.6	The Mn^{4+} Centre	156
9.6.1	Mn^{4+} Related Photoluminescence	156
9.6.2	Electron Paramagnetic Resonance of Mn^{4+}	159
9.6.3	Magnetic-Field Effects on the Mn^{4+} Related Luminescence	159
9.6.4	Dynamics of the Mn^{4+} Related Luminescence	160
9.6.5	Temperature Dependence of Mn^{4+} Centres	160
9.6.6	Mn-Mg Complexes	162
9.6.7	Resonant Stokes Process by Secondary Excitation and Stimulated Hole Transfer in Mn-Mg Complexes	171
9.7	Optical Properties as a Function of Mn Concentration and Co-Doping	177
9.8	Magnetisation of GaN:Mn	180
9.9	Conclusion	182
10	Conclusions and Future Work	184
10.1	Conclusions	184
10.2	Future Directions	185
	Bibliography	187

List of Symbols and Abbreviations

a_B	Bohr radius
arb. units	arbitrary units
BE	backscattered electron
BL	blue luminescence
CAS	calorimetric absorption spectroscopy
CB	conduction band
CCD	charge coupled device
CF	crystal field
CL	cathodoluminescence
CT	charge transfer
DAP	donor acceptor pair
DMS	dilute magnetic semiconductor
e	electron
E_b	binding energy
EMT	effective mass theory
EPR	electron paramagnetic resonance
ESEM	environmental scanning electron microscope
eV	electron volt
ε_0	vacuum dielectric constant
ε^*	effective dielectric constant in ε_0
FTIR	Fourier transform infrared
FWHM	full width at half maximum
Ga_i	gallium interstitial
h	hole
HJ	heterojunction
HV	high voltage
HVPE	hydride vapour phase epitaxy
IR	infrared
JT	Jahn-Teller effect

\vec{k}	wave vector of propagating light
LA	longitudinal acoustic
LED	light emitting diode
LO	longitudinal optical
LVM	local vibrational mode
m_0	electron mass
m_{eff}	effective mass
m^*	relative effective mass in m_0
MOCVD	metalorganic chemical vapour deposition
μ_B	Bohr magneton
pi	photoionisation
PL	photoluminescence
PLE	photoluminescence excitation
PMT	photo multiplier tube
r_B^*	effective Bohr radius
RKKY	Ruderman-Kittel-Kasuya-Yosida
SC	semiconductor
SE	secondary electron
SEM	scanning electron microscope
SIMS	Secondary ion mass spectroscopy
SO	spin-orbit interaction
SQUID	superconducting quantum interference device
σ^+	left-circularly polarised
σ^-	right-circularly polarised
T_C	Curie temperature
TA	transversal acoustic
TM	transition metal
TO	transversal optical
UV	ultraviolet
VB	valence band
Vis	visible spectral range
XRD	X-ray diffraction
YL	yellow luminescence
ZPL	zero phonon line

List of Figures

1.1	Rough outline of different models of spin-coupling in a DMS.	7
2.1	Outline of a charge transfer process	13
2.2	The term scheme of Ni^{2+} in CdS as a qualitative illustration of the emergence of the electronic structure of a TM incorporated into a hexagonal host lattice	15
2.3	Ground states and crystal field splitting of the nine 3d configurations in a crystal field of tetrahedral symmetry (T_d)	17
3.1	Charge transfer levels $\text{Fe}^{2+/1+}$, $\text{Fe}^{3+/2+}$ and $\text{Fe}^{3+/4+}$ in III-V and II-VI compounds	25
3.2	Qualitative term scheme of the Fe^{3+} centre in a tetrahedral crystal field	28
3.3	Polarised photoluminescence spectra of the $\text{Fe}^{3+} (^4T_1(\text{G}) \rightarrow ^6A_1(\text{S}))$ transition in GaN	29
3.4	Zeeman behaviour of the $(^4T_1(\text{G}) \rightarrow ^6A_1(\text{S}))$ luminescence in GaN . . .	32
3.5	X-band EPR spectrum of Fe doped GaN at 5 K for $B \parallel c$ -axis	34
3.6	Polarised luminescence spectra of the $\text{Fe}^{3+} (^4T_1(\text{G}) \rightarrow ^6A_1(\text{S}))$ transition in ZnO excited at 2.71 eV at different temperatures	35
3.7	Energy scheme of the $\text{Fe}^{3+} (^4T_1(\text{G}))$ state in a C_{3V} crystal field	36
3.8	PLE spectrum of the $(^4T_1(\text{G}) \rightarrow ^6A_1(\text{S}))$ luminescence in GaN	37
3.9	Qualitative term scheme of the Fe^{2+} centre in a tetrahedral crystal field	40
3.10	$\text{Fe}^{2+} (^5E \rightarrow ^5T_2)$ transition. Transmission spectrum of Fe-doped ZnS at $T = 4$ K	41
3.11	$\text{Fe}^{2+} (^5T_2 \rightarrow ^5E)$ luminescence in InP at $T = 4$ K	41
3.12	Theoretical splitting of the 5E and 5T_2 states in C_{3V} symmetry ignoring the Jahn-Teller effect	47
3.13	Absorption spectra of Fe doped GaP, InP and GaAs at $T = 45$ mK .	50
3.14	Absorption spectrum of Fe doped GaN at $T = 2$ K	51
5.1	SE and CL image of the GaN:Ni sample B	63
5.2	SE (a) and CL image (b) of a detail of the GaN:Ni sample B	64

5.3	CL image of the GaN:Ni sample A	65
5.4	CL spectra of Ni doped GaN samples A and B at 80 K on logarithmic scale	66
5.5	Absorbance spectra of the Ni doped GaN samples A and B	68
5.6	SE and CL image of Fe doped GaN ($[\text{Fe}] = 1 \times 10^{19} \text{ cm}^{-3}$)	70
5.7	CL spectra of GaN doped with varying concentrations of Fe	71
5.8	Micrographs of the finely structured CL pattern that shows up at low acceleration voltage in and around pits of Fe doped HVPE grown GaN [$1 \times 10^{19} \text{ cm}^{-3}$]	72
5.9	SE and CL images of two different regions of the Fe doped HVPE GaN sample [$1 \times 10^{19} \text{ cm}^{-3}$]	74
5.10	Monochromatic CL images of the area round the symmetry axis running down the $11\bar{2}2$ facets of the pits (marked by a black frame in Fig. 5.8(d)). Image (a) and (b) were recorded for an emission energy of 3.46 eV and 3.43 eV, respectively.	75
5.11	Infrared CL spectra of Fe doped GaN [$1 \times 10^{18} \text{ cm}^{-3}$] at 80 K	76
5.12	Monochromatic CL images of Fe doped GaN, [$1 \times 10^{19} \text{ cm}^{-3}$] at 1.22 eV and 80 K	76
5.13	Transmission spectra of Mn doped GaN at room temperature	78
5.14	CL spectra of Mg co-doped and non co-doped GaN:Mn at 80 K	78
5.15	PL spectrum of the GaN:Mn film on Al_2O_3 substrate at 2 K	79
5.16	Comparison of the $\text{Al}_2\text{O}_3:\text{Ti}^{3+}$ luminescence in a range of Mn doped GaN films grown on sapphire at 2 K	80
5.17	Zeeman photoluminescence spectra of the $\text{Al}_2\text{O}_3:\text{Ti}^{3+}$ luminescence in a Mn doped GaN film grown on sapphire recorded in Voigt configuration.	81
5.18	FTIR absorption spectrum of ZnO:Fe annealed in vacuum on logarithmic scale	82
6.1	X-band ($\sim 9.5 \text{ GHz}$) EPR spectrum of Fe doped GaN with a Fe concentration of $1 \times 10^{19} \text{ cm}^{-3}$ at 5 K for $\text{B} \parallel \text{c-axis}$	84
6.2	Raman spectrum of the strain-sensitive $\text{E}_2(\text{high})$ phonon mode	85
6.3	Low-temperature (2 K) luminescence of the $\text{Fe}^{3+} (^4\text{T}_1(\text{G}) \rightarrow ^6\text{A}_1(\text{S}))$ transition in GaN for different Fe concentrations	86
6.4	Polarised high resolution PL spectra of the $(^4\text{T}_1(\text{G}) \rightarrow ^6\text{A}_1(\text{S}))$ ZPL of Fe^{3+} in GaN at $\text{T}=2 \text{ K}$, $[\text{Fe}]=1 \times 10^{19} \text{ cm}^{-3}$	87
6.5	Splitting of the $^4\text{T}_1(\text{G})$ state in trigonal $\text{C}_{3\text{V}}$ symmetry, derived from the fine structure of the $(^4\text{T}_1(\text{G}) \rightarrow ^6\text{A}_1(\text{S}))$ luminescence (Fig. 6.4)	88

6.6	Concentration dependency of the $\text{Fe}^{3+}({}^4\text{T}_1(\text{G})\text{—}{}^6\text{A}_1(\text{S}))$ luminescence	89
6.7	PL difference spectrum of the sideband of the Fe^{3+} emission in GaN	91
6.8	EPR spectra of Fe doped GaN, $[\text{Fe}]=1\times 10^{19} \text{ cm}^{-3}$, 9.49 GHz and 4 K. Stackplot for rotation of the magnetic field	93
6.9	Optical transmission spectra of Fe-doped GaN with different concentrations of iron at 2 K	95
6.10	Optical UV transmission spectrum of GaN with $[\text{Fe}]=1\times 10^{19} \text{ cm}^{-3}$ at 2 K and $\vec{k} \parallel \text{c-axis}$	99
6.11	Term scheme of Fe^{3+} in GaN	101
6.12	PLE spectra of the $\text{Fe}^{3+}({}^4\text{T}_1(\text{G})\text{—}{}^6\text{A}_1(\text{S}))$ luminescence at 1.299 eV of Fe doped GaN at 7 K on logarithmic scale	102
6.13	Energy scheme of the creation of free holes via deep defects involved in the intrinsic yellow luminescence in GaN	104
6.14	Low temperature FTIR transmission spectra of Fe doped GaN for different Fe concentrations	107
6.15	Detailed analysis of the intra-centre Fe^{2+} transition, (${}^5\text{E}\text{—}{}^5\text{T}_2$), in GaN with $[\text{Fe}]=1\times 10^{18} \text{ cm}^{-3}$ by means of FTIR transmission spectroscopy at different temperatures and polarisation	109
6.16	Term scheme of Fe^{2+} in GaN including most of the splitting caused by the trigonal distortion due to the $\text{C}_{3\text{V}}$ -symmetry	111
7.1	Temperature dependent calorimetric absorption spectra of the fine structure lines ($\text{a}'\text{—e}'$) and (a,b) representing transitions $\text{Fe}^{3+}\rightarrow[\text{Fe}^{2+}({}^5\text{E}),\text{h}]$ at mK-temperatures	116
7.2	Sketch of an absorption transition with a two-fold split ground state and one excited state.	117
7.3	Temperature dependance of the seven fine structure lines ($\text{a}'\text{—e}'$) and (a,b) observed in semi-insulating GaP and InP (Fig. 7.1)	118
7.4	Exemplary absorption spectra of the quintet ($\text{a}'\text{—e}'$) in GaP and InP under different uniaxial pressure conditions.	120
7.5	Pressure-behaviour of quintet ($\text{a}'\text{—e}'$) (from bottom to top).	121
7.6	Stress behaviour of lines a , b , A , A_1 in InP	122
7.7	Symmetries and relative energies of $[\text{Fe}^{2+}({}^5\text{E}),\text{h}]$ states under consideration of weak and strong exchange interaction between the $\text{Fe}^{2+}({}^5\text{E})$ spin-orbit states and the $\Gamma_8\text{-VB-hole}$	123
7.8	Comparison and association of the fine structure lines of the $(\text{Fe}^{2+}({}^5\text{E}),\text{h})$ complex with EMT states	126

7.9	Assignment of the fine structure lines of the $(\text{Fe}^{2+}({}^5\text{T}_2), \text{h})$ complex to EMT states of the hole	127
7.10	Assignment of the CT lines found in Fig. 3.13 to bound states that are characterised by the electronic state of the involved Fe^{2+} centre and an EMT state	130
8.1	FTIR absorption spectra of the four ZnO samples at 1.8 K and 60 K on logarithmic scale	132
8.2	Comparison of the $\text{ZnO}:\text{Fe}^{2+}({}^5\text{E}—{}^5\text{T}_2)$ spectra of the Zn- and the vacuum annealed samples at 1.8 K displayed on logarithmic scale . .	135
8.3	Polarised spectra of the $\text{ZnO}:\text{Fe}^{2+}$ absorption and its sideband at 1.8 K for the Zn-annealed and the vacuum-annealed crystal on logarithmic scale	136
8.4	Temperature resolved FTIR absorption spectra of $\text{ZnO}:\text{Fe}$ annealed in Zn atmosphere	139
8.5	Temperature resolved FTIR absorption spectra of $\text{ZnO}:\text{Fe}$ annealed in Zn atmosphere	140
9.1	Summary of the current state of research regarding the gap states formed by Mn in GaN	146
9.2	High resolution XRD scans of undoped GaN, Mn doped GaN (1.5 %), Si co-doped GaMnN (1.5 %, $1 \times 10^{19} \text{ cm}^{-3}$)	147
9.3	Raman spectra of GaN doped with Mn at concentrations ranging from 0 % to 1.5 % at room temperature	148
9.4	Absorption spectrum of Mn doped GaN ($[\text{Mn}] \sim 1 \times 10^{20} \text{ cm}^{-3}$) at room temperature	150
9.5	PL spectra of $(\text{Ga}, \text{Mn})\text{N}$ samples on sapphire at $T = 2 \text{ K}$ excited at 2.41 eV	151
9.6	PL spectrum of the $\text{Mn}^{3+}({}^5\text{E}—{}^5\text{T}_2)$ transition in GaN with a Mn concentration of around 0.03 % at $T = 2 \text{ K}$ on logarithmic scale . . .	152
9.7	Zeeman transmission spectra of the $\text{Mn}^{3+}({}^5\text{T}_2—{}^5\text{E})$ transition in Faraday and Voigt configuration at 2 K	153
9.8	EPR spectra of $\text{Ga}_{0.985}\text{Mn}_{0.015}\text{N}:\text{Si}$ ($[\text{Si}] = 2 \times 10^{19} \text{ cm}^{-3}$) recorded in the X-band ($\sim 9.49 \text{ GHz}$) with the magnetic field oriented parallel and perpendicular to the c-axis at 5 K	154
9.9	Breit-Rabi diagram of Mn^{2+} in a hexagonal crystal under the influence of a magnetic field parallel to the c-axis	155
9.10	PL spectra of $\text{GaN}:\text{Mn}$ co-doped with Mg at $T = 1.8 \text{ K}$	157

9.11	PL spectra of the same luminescence as in Fig. 9.10 excited at different energies at $T = 20$ K. From [1]	158
9.12	Zeeman PL spectra of the alleged Mn^{4+} luminescence from Fig. 9.10	160
9.13	Temperature dependent PL spectra of the alleged Mn^{4+} luminescence	161
9.14	PLE spectra of the Mn^{4+} luminescence (top) on logarithmic scale with detail on linear scale. Mg co-doped GaN:Mn.	163
9.15	PLE spectra of the Mn^{4+} luminescence (top) on logarithmic scale with detail on linear scale. Non co-doped GaN:Mn.	164
9.16	PLE spectra of the Mn^{4+} luminescence versus the energy difference from the detection. Mg co-doped GaN:Mn.	165
9.17	PLE spectra of the Mn^{4+} luminescence versus the energy difference from the detection. Non co-doped GaN:Mn	166
9.18	Energy diagram of the excitation process via the $\text{Mn}^{4+} \rightarrow \text{Mn}^{3+}$ CT resulting in excited Mn^{4+}	169
9.19	Temperature dependent PLE spectra of the Mn^{4+} luminescence shown in Fig. 9.17	172
9.20	Room temperature PLE spectrum of the Mn^{4+} luminescence shown in Fig. 9.15	173
9.21	Excitation selective PL spectra at room temperature.	174
9.22	Summary of Fig. 9.21	175
9.23	Energy diagram of the excitation mechanism behind the intense resonance found in the PLE spectra of the Mn^{4+} luminescence	176
9.24	Compilation of PL, absorption and EPR spectra for GaN with different Mn doping and co-doping	178
9.25	Magnetisation of $\text{Ga}_{1-x}\text{Mn}_x\text{N}$ as a function of an external magnetic field at room temperature	181
9.26	Comparison of the magnetisation characteristic of non co-doped and Mg co-doped GaN:Mn at room temperature	181

List of Tables

2.1	Nomenclature of TM ions regarding neutral and ionised donors and acceptors	11
2.2	Selection rules for optical transitions in T_d symmetry	21
2.3	Selection rules for electronic dipole transitions in C_{3V} -symmetry . . .	21
3.1	Experimentally determined position of the CT levels $Fe^{3+/2+}$ and $Fe^{2+/1+}$	26
3.2	Observations on the $Fe^{3+}(^4T_1(G) \rightarrow ^6A_1(S))$ luminescence: Energy, FWHM, lifetime and the fine structure of the involved states	30
3.3	Ligand field parameters for the spin-Hamiltonian of the $^6A_1(S)$ state determined from Zeeman and EPR experiments	33
3.4	The $(^5E \rightarrow ^5T_2)$ transition and derived crystal field and spin-orbit coupling parameters Dq and λ for various cubic (c) and wurtzitic (h) host materials	43
3.5	TA(L) phonon energies $\hbar\omega$ and Jahn-Teller energies E_{JT} used to model the $Fe^{2+}(^5E)$ fine structure in various host materials	44
4.1	Resistivity of Fe doped GaN samples measured by ATMI at room temperature.	54
6.1	Sideband of $Fe^{3+}(^4T_1(G) \rightarrow ^6A_1(S))$ luminescence	90
6.2	Sharp lines associated with Fe-complexes and their polarisation . . .	92
6.3	Absorption lines found in UV-VIS-Transmission spectra at 2 K with the polarisation given in brackets	96
6.4	Energy E , favoured polarisation and thermalisation behaviour of the absorption lines observed in Fig. 6.15	110
7.1	Parameters of Eq. 7.2 determined by fitting the temperature dependencies of lines (a'-e') and (a,b) in Fig. 7.3.	119
8.1	Comparison of high energy lines found for the Fe^{2+} centre with the energy of defect modes related to other impurity centres.	138